Materials Science & Engineering C 129 (2021) 112388

Contents lists available at ScienceDirect

Materials Science & Engineering C

journal homepage: www.elsevier.com/locate/msec

# Microfluidic devices manufacturing with a stereolithographic printer for biological applications

Bastián Carnero [a], Carmen Bao-Varela [a], Ana Isabel Gómez-Varela [a], Ezequiel Álvarez [b,c,d], María Teresa Flores-Arias [a,*]

[a] Photonics4Life Research Group, Applied Physics Department, Facultade de Física and Facultade de Óptica e Optometría, Universidade de Santiago de Compostela, Campus Vida, E-15782 Santiago de Compostela, Spain
[b] Cardiology Group, Health Research Institute of Santiago de Compostela (IDIS), University Hospital of Santiago de Compostela (SERGAS), Trav. Choupana s/n, E-15706 Santiago de Compostela, Spain
[c] Centro de Investigación Biomédica en Red de Enfermedades Cardiovasculares (CIBERCV), Madrid, Spain
[d] Department of Pharmacology, Pharmacy and Pharmaceutical Technology, Universidade de Santiago de Compostela, E-15782 Santiago de Compostela, Spain

ARTICLE INFO

*Keywords:*
Stereolithography
Low force stereolithography
Microfluidics
Organ-on-a-chip
3D printing
Microchannel
Pillar
Soft lithography
PDMS
Biocompatibility
HUVEC

ABSTRACT

Stereolithographic printers have revolutionized many manufacturing processes with their capacity to easily produce highly detailed structures. In the field of microfluidics, this technique avoids the use of complex steps and equipment of the conventional technologies. The potential of low force stereolithography technology is analysed for the first time using a Form 3B printer and seven printing resins through the fabrication of microchannels and pillars. Manufacturing performance of internal and superficial channels and pillars is studied for the seven printing resins in different configurations. A complete characterization of printed structures is carried out by optical, confocal and SEM microscopy, and EDX analysis. Internal channels with unobstructed lumen are obtained for diameters and angles greater than 500 μm and 60°, respectively. Outward and inward superficial channels in the range of hundreds of microns can be fabricated with an accurate profile, printing them with a perpendicular orientation respect to the base, allowing a proper uncured resin evacuation. Outward channels are replicated by soft lithography using polydimethylsiloxane. Clear, Model and Tough resins show a good behaviour to be used as master, but Amber and Dental resins present a poor topology transference from the master to the replica. According to the needs of devices used for biological and biomedical research, transparency as well as superficial biocompatibility of some resins is evaluated. Human umbilical vein endothelial cells (HUVEC) adhesion is confirmed on Amber, Dental and Clear resins, but these cells were only able to grow and progress as a cell culture over the Amber resin. Therefore, Amber showed an adequate biocompatibility, in terms of cell adhesion and growth for HUVEC.

## 1. Introduction

3D printing has evolved to become one of the most revolutionary manufacturing techniques. The capacity to directly and consistently produce highly detailed structures without involving many of the usual steps or equipment of conventional technologies has democratized the access to the manufacturing process to a vast quantity of industries, researchers and individuals [1,2]. The microfluidics field is no stranger to the impact that 3D printing can have in its microfabrication procedures [3,4], mainly dominated by techniques as photolithography or Reactive Ion Etching (RIE), that usually require the use of very specific facilities and produce a highly polluting chemical waste [5,6]. In this field, one of the main goals is to fabricate complex devices that mimic, for instance, different structures of the human body (organ-on-a-chip), by combining superficial (inward and outward) and internal channels with several kind of pillars [7,8]. This is where 3D printing stands out as it makes possible, with a user-friendly equipment and software, the realization of 3D structures in volume with great structural complexity.

Two 3D printing technologies can be highlighted from the rest [3]: Fused Deposition Modelling (FDM) [9] and Stereolithography (SLA). On one hand, FDM printers rely on the precise deposition of a polymeric filament previously heated and extruded in consecutive layers to form

* Corresponding author.
*E-mail address:* maite.flores@usc.es (M.T. Flores-Arias).

https://doi.org/10.1016/j.msec.2021.112388
Received 4 May 2021; Received in revised form 27 July 2021; Accepted 17 August 2021
Available online 26 August 2021

the designed piece (Fig. 1a). On the other hand, SLA printers utilize the photopolymerization principle to perform a layer-by-layer cure of a liquid resin deposited in a tank (Fig. 1b).

Both technologies have been proven to be as versatile as efficient and are widely used, although SLA printers are beginning to gain ground in technical areas where accuracy is critical [10,11]. Once the light source (generally a laser) with the smallest possible spot and the appropriate resin has been selected, surface quality can be improved by controlling piece orientation. There are infinite ways to orient a piece to be printed, so a detailed study of the influence of the slope of the faces in the photopolymerization process is interesting to know the optimal configurations. The key idea to understand this influence is that a rotation in the piece will modify the way in which the printer slices the original object [12]. Therefore, objects with great surface detail can be printed at an angle that favours the precise curing of their constituent layers. The same applies to internal channels, where a suitable angle could help the removal of uncured resin from inside, helping to avoid obstructions.

In addition to the high superficial quality that SLA printers offer, biocompatible materials that can be printed with this equipment have been developed, increasing the number of potential biological applications. In this field, researchers have printed a bioresorbable airway splint [13], a $H_2O_2$ and glucose detection device [14] or 3D scaffolds [15] and platforms [16] for cell seeding. All these examples show the potential of SLA printers for the fabrication of complex microfluidic devices for biological usage, and make them a good choice for researchers focused on 3D printing of accurate, reliable, and biologically solvent microfluidic devices [17,18].

This work presents a detailed study of microfluidic devices that can be fabricated by Low Force Stereolithography (LFS) technology to be used as Organ-On-A-Chip (OOC) or as master to replicate OOC in other biocompatible material. The LFS is an SLA technique that combines a galvanometer system that directs the laser beam with a spatial filter, a fold, and a parabolic mirror to deliver the beam perpendicular to the resin tank. This technique improves the precision and accuracy of the OOC fabricated, since a more uniformity deposition of laser energy across the built-in platform is obtained.

A complete and detailed analysis of the printer performance is carried out for the first time, to our knowledge, for LFS technique, by testing the printing results of seven compatible resins (three of them being biocompatible). Both printing time and light transmittance of each of the resins are determined due to their relevance to the fabrication process. The formation of internal channels is assessed since LFS stands out over photolithography, RIE (allowing the formation of internal cavities of a vast quantity of orientations and geometries) and other SLA printers (granting the perpendicular focus of the beam) for this functionality. The range of dimension of different kind of channels and pillars that can be accurately fabricated is evaluated. Furthermore, the finishing and precision of inward and outward superficial channels and pillars are analysed at the maximum resolution allowed for each resin. The replicability of all the resins by soft lithography of polydimethylsiloxane (PDMS) is also studied since the printed structures are of great interest for the manufacture of masters [19,20]. Finally, the biocompatibility of the selected resins is analysed using human endothelial cells.

## 2. Materials and methods

### 2.1. 3D printing

The Form 3B printer (Formlabs, Somerville, Massachusetts) used in this work offers a novel feature over other stereolithographic printers by two aspects: allowing the printing of biocompatible resins and employing a new photopolymerization process called Low Force Stereolithography (LFS) [21]. This technique has been designed to reduce the manufacturing stresses that the pieces suffer during the printing process. For this, a resin tank with a flexible sheet at its base is used. This base gradually deforms when the piece is pressed against it. For the polymerization of the resin, the laser is always addressed perpendicular to the piece thanks to a galvanometric system consisting of a fold mirror and a parabolic mirror.

To analyse the maximum resolution that can be reached for each of the resins, plates of 3 × 4 cm with a series of channels and pillars on their surface were designed using a CAD-like software (Fig. 2a). Channels were printed outwards and inwards from the surface and with two different profiles: rectangular (from 50 μm to 1000 μm width) and semicircular (from 30 μm to 750 μm radius). Pillars (outward) and wells (inward) were also printed (from 100 μm to 1600 μm height). Each plate was printed with three different orientations (Fig. 2b) respect to the base of the printing arm: at 0° (Fig. 2c), at 45° with channels parallel to the y axis (Fig. 2d) and at 45° with channels contained in the XZ plane (Fig. 2e). We will call these orientations A, B and C, respectively, to facilitate further discussion. To study the influence of the printing angle on the ability to create internal channels and to analyse if this printer presents more advantages than others, a quarter annulus crossed by seven internal channels oriented at 0°, 15°, 30°, 45°, 60°, 75° and 90° was printed (Fig. 2f), as it was done by previous authors [12]. This study was performed four times for each resin selected, also varying the diameter of the channels from 250 μm to 1500 μm. Last, round discs with 3.5 cm of diameter and 5 mm of height (Fig. 2g) were printed to perform optical and biocompatibility studies on the surface of resins, by studying cell proliferation under static conditions. A two-step polishing process was carried out after fabrication to one or both faces of the discs in order to evaluate the difference in the transmission spectra, employing a Logitech PM 2A (Logitech, Lausanne, Switzerland) polisher. First, an iron disc plate and an abrasive solution of $Al_2O_3$ were used to perform the roughing. The second step was the optical polishing of the material combining an expanded polyurethane disc with an OCON 140 silica

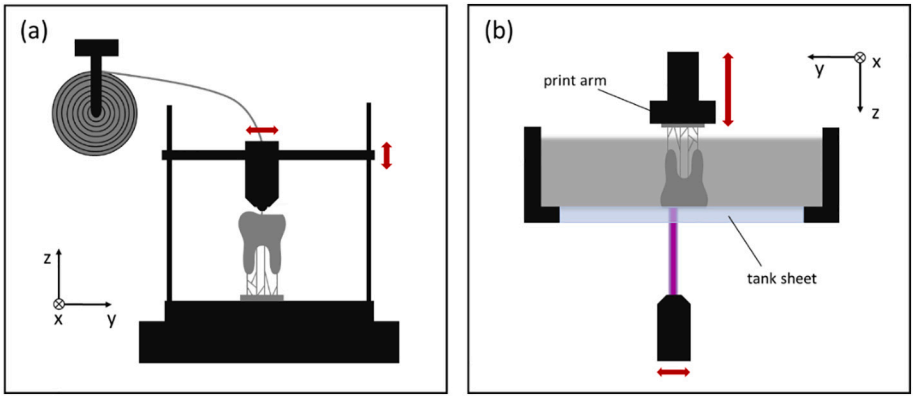


**Fig. 1.** The most common 3D printing techniques: (a) fused deposition modelling (FDM) and (b) stereolithography (SLA).

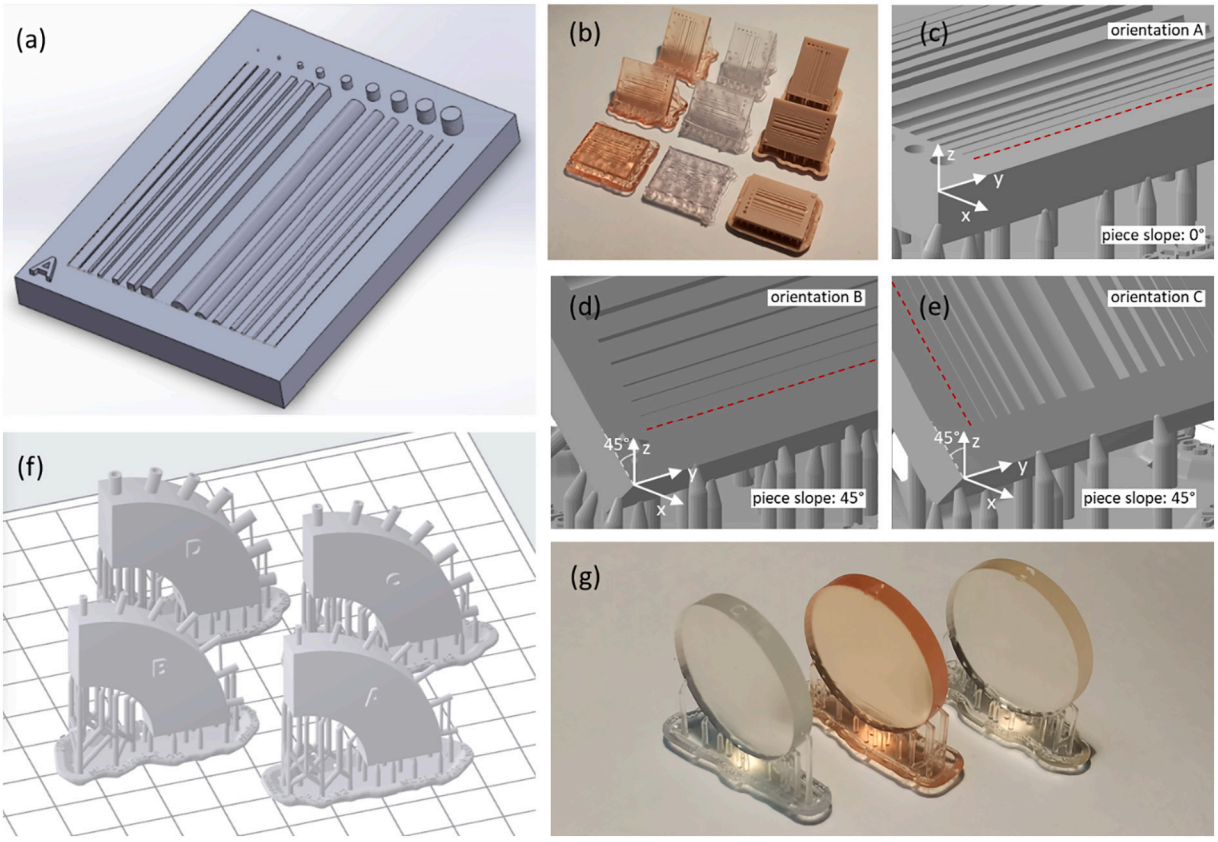


**Fig. 2.** 3D pieces printed in this work. (a) CAD design of the plates with the outward channels and pillars. (b) Picture of three sets of plates with the inward channels and pillars printed in different orientations for three kinds of resins (from left to right: Amber, Flexible and Model, see Section 2.2). Images of CAD corresponding to the different printing orientations of the plates: at (c) 0° (orientation A), (d) at 45° with channels parallel to the y axis (orientation B), and (e) at 45° with channels contained in the XZ plane (orientation C). (f) Quarter annulus designed to analyse the capacity of the printer to manufacture internal channels. (g) Picture of round discs printed for biocompatibility and optical quality studies. Notice the presence of typical scaffolding to support the structures.

solution.

It is necessary to postcure the pieces in a two-step process. First, the piece is washed in isopropanol (IPA) >90% inside the Form Wash tank (Formlabs, Somerville, Massachusetts) during the corresponding time recommended by the manufacturer for each resin, which usually ranges from10 to 20 min. This process can be carried out in one or two stages depending also on the resin. Secondly, the pieces are left to dry and introduced into the UV Form Cure chamber (Formlabs, Somerville, Massachusetts). This chamber is provided with LEDs emitting at 405 nm and also allows to control the temperature. Curing temperatures range from 60 to 80 °C and curing times from 10 to 60 min for the selected resins.

### 2.2. Materials

Seven stereolithography resins from Formlabs were analysed: Clear V4, Dental LT V1, Tough 2000 V1, BioMed Amber V1, Flexible 80A V1, Elastic 50A V1 and Model V2. One of the most critical parameters when studying the resolution and surface finishing of the prints is the layer height (z-step) that every resin admits. In order to achieve the optimal performance in each case, the pieces were always printed with the maximum resolution (minimum z-step) available for each of the resins. Thereby, the theoretical Minimum Thickness of the Layer (MTL) was 25 μm for Clear and Model resins; 50 μm for Tough, Amber and Flexible; and 100 μm for Elastic and Dental.

The PDMS was prepared from Sylgard 184 elastomer (Dow Chemical Company, Midland, Michigan) and selected as the polymer to carry out the replication studies given its optical transparency, permeability to gases, elasticity, and biocompatibility. PDMS is one of the most used polymers to fabricate microfluidic devices [22,23], allowing the cells to have a suitable environment for experimentation, and was synthesized by mixing the monomer and the curing agent in a ratio 10:1 (according to the supplier specifications). The mixture was then deposited on the printed plates inside a Petri dish, forming a small silicone sheet and introduced in a vacuum chamber 40 min at 400 mbar to remove bubbles produced during the mixing process. Finally, the Petri dish with the degassed PDMS was cured in an oven for 12 h at 60 °C.

The biocompatibility of the previous resins and PDMS, as well as the corresponding disinfection or sterilization protocols given by the manufacturer are shown in Table 1.

### 2.3. Cell cultures

Human umbilical vein endothelial cells (HUVEC) were isolated from freshly obtained human umbilical cords donated under informed consent from mothers, and following the method previously described [24]. HUVEC were selected because they are a primary cell culture (more sensitive than a cell line for cytotoxicity assays), from human origin, and because they are the cells that cover all the inner surface of vascular bed, and any implanted device must be “reendothelized” to avoid blood clotting. All the procedures were approved by the Ethics Committee for Clinical Research at Galicia (Spain; Registry no. 2110/2019), according to the World Medical Association Declaration of Helsinki. Briefly, HUVEC were cultured on 0.2% (w/v) Sigma-Aldrich gelatine (Merck Life Science S.L.U., Madrid, Spain) pre-coated flasks or dishes (Corning, New York, New York) and grown in complete Endothelial Growth Medium-2 media (Lonza, Basel, Switzerland), containing 2% foetal bovine serum (FBS) and gentamicin/amphotericin B between other

**Table 1**
Manufacturer properties of the different resins used in our study and for PDMS. The autoclavable pieces underwent 5 cycles of pre-vacuum steam sterilization at 132 °C with a 4-minute sterilization phase and 30 min dry phase. Pieces were allowed to cool 30 min between cycles. *In this work, Dental resin was autoclaved once without showing deterioration.

| Resine | Biocompatible | Sterilizable | Disinfectable | Transparency | Method of sterilization/disinfection |
|---|---|---|---|---|---|
| Clear V4 | ✓ | ✓ | ✓ | ✓ | Autoclavation |
| BioMed Amber V1 | ✓ | ✓ | ✓ | ✓ | Autoclavation |
| Dental LT V1* | ✓ | × | ✓ | ✓ | 70% IPA for 5 min |
| Elastic 50A V1 | × | ✓ | ✓ | ✓ | Autoclavation |
| Tough 2000 V1 | × | × | × | × | – |
| Model V2 | × | × | × | × | – |
| Flexible 80A V1 | × | × | × | ✓ | – |
| PDMS | ✓ | ✓ | ✓ | ✓ | Autoclavation |

components, in a humidity-saturated atmosphere with 5% $CO_2$ at 37 °C. Cells for the experiments were used between the second and seventh passages to maintain HUVEC phenotype.

For the biocompatibility experiments, HUVEC were cultured under standard conditions over the discs printed using the three biocompatible resins, after sterilization and pre-coating of the surfaces with 0.2% (w/v) gelatine. HUVEC were seeded at a density of 10,000 cells/$cm^2$ for all the cases. Standard polystyrene plates (Corning, New York, New York) in the same conditions were used as control experiments. HUVEC adhesion was checked 4 h after cell seeding in an inverted microscope, and cell viability was tested with living cells staining calcein acetomethylester (AM) (Invitrogen, Thermo Fischer Scientific, Waltham, Massachusetts) at 4 and 24 h. For this, calcein AM at a concentration of 1 μM in phosphate buffer solution (PBS) was incubated with the cells for 15 min in the dark at 37 °C, and then, the excess of calcein was removed with two washes of PBS. Images from the cultures were obtained with a fluorescent microscope and used to inspect cell viability and count the cells to quantify cell growing. Three to five images (800 × 600 μm) from each cell culture were taken from at least three independent experiments. Images were also processed with ImageJ (https://imagej.nih.gov/ij/index.html) to estimate the surface area of the cells. The growth of the cultures was quantified by the percentage of increased number of cells after 24 h.

### 2.4. Data collection

Confocal images of the microchannels manufactured on the plates and superficial roughness measurements were obtained using a 3D optical profilometer S neox (Sensofar Metrology, Terrassa, Spain). A Nikon MM-400 metallurgic microscope (Nikon Instruments Europe B.V., Amsterdam, The Netherlands) was used when the depth of the channel was too large for confocal inspection, as is the case with internal channels. To measure the transmission spectra of the transparent resins, a PerkinElmer Lamb25 spectrometer (PerkinElmer Inc., Waltham, Massachusetts) was used. This spectrometer performed a measurement of the transmittance of the disc between 190 nm and 1100 nm, in 1 nm intervals. Furthermore, a Field Emission Scanning Electron Microscope (FESEM; Zeiss, Oberkochen, Germany) was used to make the SEM images presented in the work. The possible transference of material from the master to the replica was evaluated by Energy Dispersive X-Ray (EDX). HUVEC adhesion was checked in a Leica DMIL inverted phase contrast microscope (Leica Microsystems AG, Wetzlar, Germany) with a digital camera EC3 (Leica Microsystems AG, Wetzlar, Germany). Finally, the fluorescence images of the cell cultures were acquired using an inverted fluorescence microscope Zeiss Axio Vert.A1 (Zeiss, Oberkochen, Germany).

## 3. Results and discussion

### 3.1. Printing time

To evaluate the possibility of implementing this technique in a mass production system, the printing time of the different resins was compared since it can be decisive if the process wants to be exploited in the industry. The time employed for printing the same set of pieces (consisted of the three orientation study plates (Fig. 2b) and the four internal channels study annulus (Fig. 2f) was measured for each resin, facilitating direct comparison. Even though the pieces were the same, the printer used a different volume for each resin. Each piece was printed with the MTL allowed for the selected resin. Table 2 shows the parameters described above as well as the ratio between the volume (V) of resin used and the printing time (t).

Dental resin proves to be the fastest printing, with a V/t ratio of 227 μl/min, followed by Amber resin, with a ratio of 106 μl/min. It can be observed that the resolution is not decisive in the printing time since resins with a lower MTL can be printed in less time than resins with a higher MTL. This occurs with Flexible and Amber resins, which despite having both a resolution of 50 μm, take less time to print the same piece than in the case of Tough, with 100 μm resolution. However, Model and Clear resins, with a resolution of 25 μm, take the longest time to print.

### 3.2. Resins transmission spectra

Optical transparency is another key property to consider when selecting a particular resin for the fabrication of microfluidic devices where optical inspection is necessary. Transparency allows the possibility of using optical images systems for inspection in different applications, for example, bright field or fluorescence images [25].

The discs printed for the biocompatibility studies were inserted in the spectrometer to measure the transmission spectra of the five transparent resins: Amber, Clear, Dental, Flexible and Elastic (see Table 1). A polishing treatment was carried out on the transparent resins that allowed it (Clear, Dental and Amber), to analyse its influence on the optical quality. Elastic and Flexible resin discs were proven to be very difficult to polish, as they showed great deformability. The polishing of the discs has a great influence on its surface roughness, that in this work was measured using the arithmetical mean roughness of the surface ($S_a$), according to ISO 25178. For this purpose, areas of equal size (1 $mm^2$) were analysed before and after polishing, respectively. The results showed that $S_a$ went from 1.977 ± 0.187 μm to 0.239 ± 0.018 μm in the case of Amber resin; from 1.281 ± 0.306 μm to 0.214 ± 0.013 μm in the case of Clear resin, and from 4.296 ± 1.047 μm to 0.242 ± 0.028 μm in the case of Dental resin.

**Table 2**
Printing time, volume and MTL of the resins used in this study.

| Resine | Time (min) | Volume (ml) | V/t (μl/min) | MTL (μm) |
|---|---|---|---|---|
| Model | 829 | 37 | 45 | 25 |
| Clear | 731 | 42 | 57 | 25 |
| Tough | 600 | 42 | 70 | 50 |
| Elastic | 585 | 42 | 72 | 100 |
| Flexible | 561 | 43 | 77 | 50 |
| Amber | 360 | 38 | 106 | 50 |
| Dental LT | 163 | 37 | 227 | 100 |

Fig. 3a–c shows the transmittance curves obtained for discs with different polished faces. All the resins show a total absorption in the ultraviolet wavelength range. The transmittance increases as the wavelength increases from visible to near infrared wavelength range (400–1100 nm). In the case of Amber, a peak of absorption appears at 550 nm. For the Clear and Dental resins two absorption peaks appear at 900 nm and 1010 nm. The total transmittance experiments an increase of around 20% when both faces are polished, with the three resins reaching a very similar transmittance for this case. Dental resin shows the greatest transmittance in the visible range (where excitation wavelengths are normally found in fluorescence microscopy), reaching 60% for 430 nm and achieving up to 80% for 750 nm. Otherwise, Amber and Clear resins show a 60% transmittance for wavelengths around 465 nm, but both reach 80% for 750 nm. As a great absorption is not observed near the excitation wavelengths of fluorescence imaging systems, typically located around 480 nm, these resins are suitable to be used with them. In the near-infrared range, the transmittance is very high and never lower than 80% once both sides are polished.

In the case of Flexible and Elastic resins (Fig. 3d), the measured transmittance was low, not reaching 40% for the visible spectrum. Moreover, transmittance cannot be improved by an easy polishing process due to their elasticity. This makes their use undesirable as resins for making microfluidics devices that need optical inspection.

### 3.3. Internal channels

Manufacturing continuous internal channels with an unobstructed lumen is one of the actual challenges for the SLA printers due to the great potential in microfluidics. The formation of internal cavities is very complex given the photopolymerization operating principle, in which each of the layers that make up a piece is supported by the previous ones. This fact explains the need for printers of this type to manufacture scaffolds that support the tilted or highly curved regions of the design. The objective of obtain unobstructed channels clashes with the need for the printer to form scaffolds, so that many internal channels are printed without the necessary supports and end up collapsing. In addition, for channels that do not pose a structural challenge given their small size, the limiting factor turns out to be the own printer resolution. To analyse the influence of the printing angle on the internal channel performance of the printer, four quarter annuli were printed per resin, each with four different channel diameters.

Three printing regimes were observed. For small diameters (250 μm), no channel was formed for any of the resins, so it can be concluded that for these sizes, the resolution of the printer does not allow the formation of internal cavities.

For medium diameters (500–1000 μm), channels begin to form (see Fig. 4a and b). The end of these channels was measured, and the accuracy was defined as the percentage ratio between the printed diameter and the designed one. In general, the trend observed is an increase in diameter as the printing angle increases, for a same designed value. In the case of channels of 500 μm in diameter, Amber and Dental resins almost reach the 100% accuracy for an angle of 90°. For lower angles, the channels get narrower (Fig. 4d) and incomplete (longitudinally), closing until disappearing at 0°. Amber resin allows to form complete channels for 60°, 75° and 90° while Clear and Dental only for 90°. For the other cases, the channels do not get to form completely, with a length that increases with the angle. For channels of 1000 μm in diameter, the printing precision increases globally, being always above 70%. A larger angle continues to improve accuracy (Fig. 4e and f) and for 90°, almost all the resins are above 90%.

For wide diameters (1500 μm), an accuracy of over 85% was reached for all channels (Fig. 4c). The length of the channels also increases, forming completely from 15° for Amber and Dental resin and from 45° for Clear resin. This can be considered the optimal internal channel size because it allows the formation of cavities inside the volume at every angle without the need for scaffolding inside it, since its small size does not pose a structural risk. For channels below this diameter and above 250 μm, the angle is the limiting factor, since it favours the adequate removal of uncured resin from the interior of the channels, whose viscosity can cause it to get trapped inside.

### 3.4. Superficial structures

Superficial channels are the basic element in essentially all microfluidics devices. They are responsible for guiding the fluid through the valves, mixers or pumps that make up the system and correct operation will depend on their quality. Thereby, a suitable channel for microfluidics will have a regular and continuous profile, accurate size and must be manufactured in the most suitable material depending on its application. The same occurs for wells, that can be used as repositories,

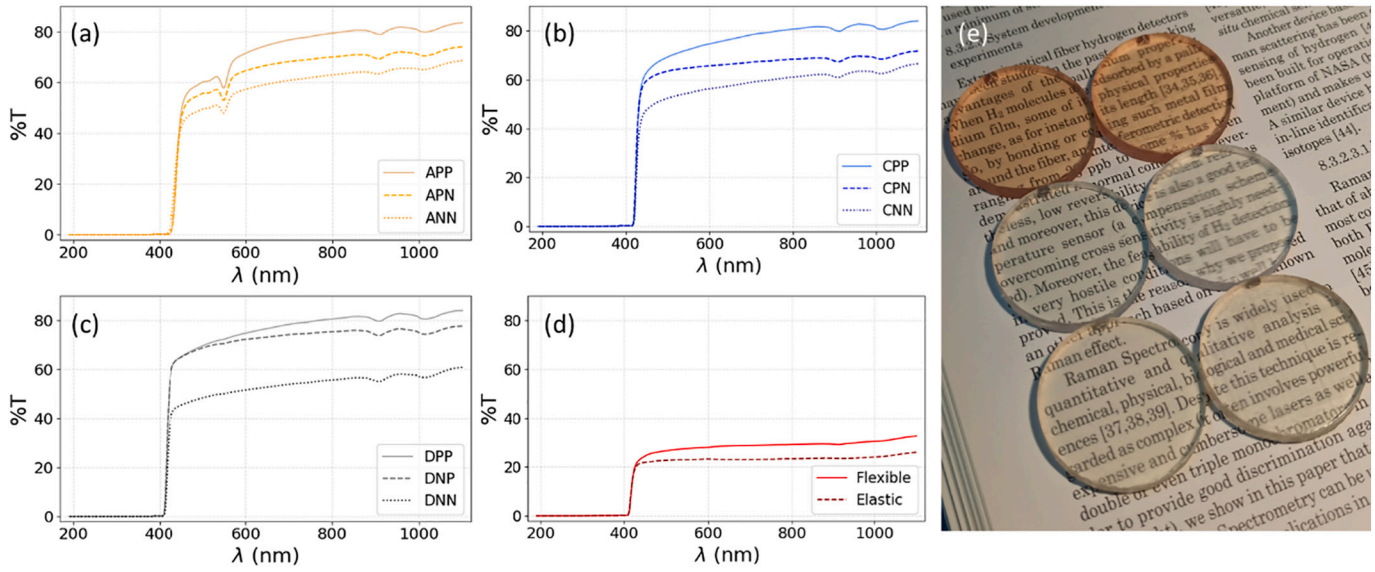


**Fig. 3.** Transmittance curves obtained for the resins: (a) Amber, (b) Clear, (c) Dental, (d) Flexible and Elastic. (e) Visual inspection of the transparency achieved by the discs of the three resins with both (left) and neither (right) face polished. NN: Neither face polished (solid line); NP: a face polished (dashed line); and PP: both faces polished (dotted line).

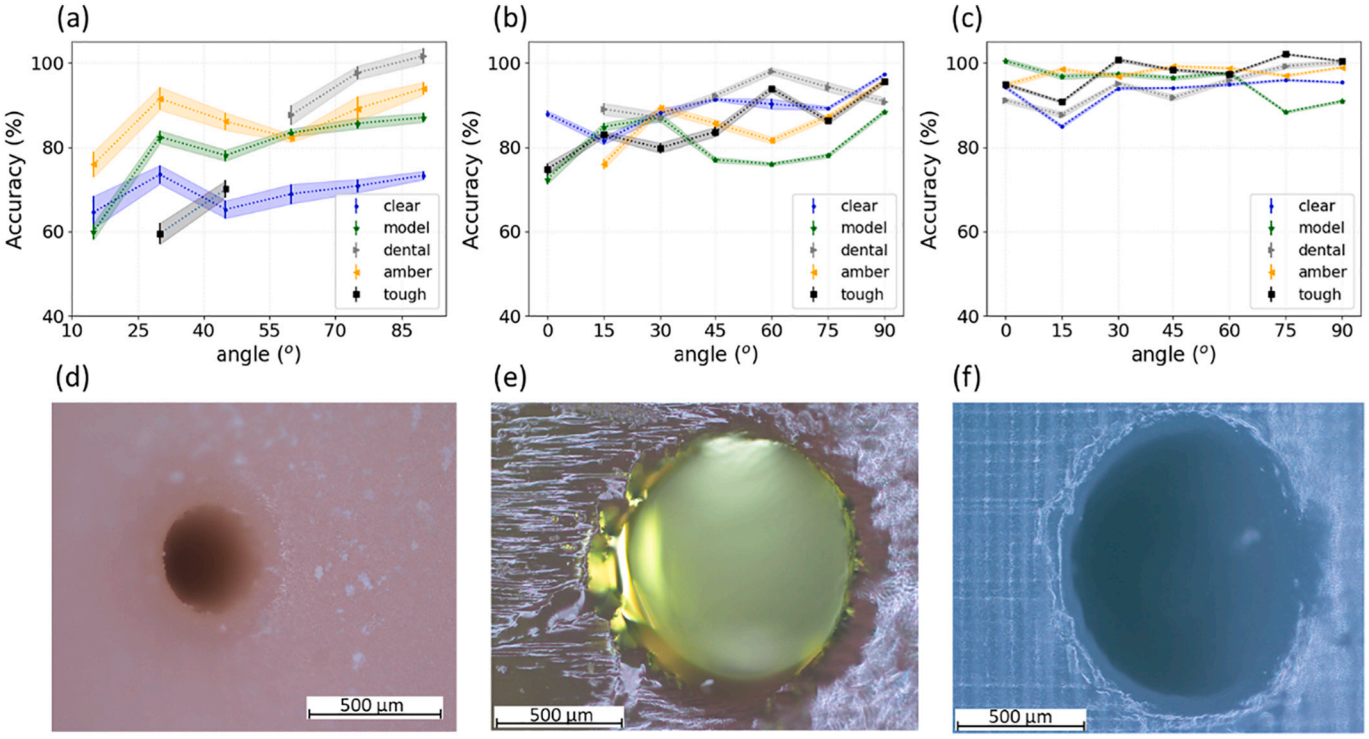


**Fig. 4.** Printing accuracy of internal channels designed with (a) 500 µm, (b) 1000 µm and (c) 1500 µm in diameter. Microscope images of selected end of internal channels printed using various resins, angles, and theoretical diameters: (d) Model, 60°, 500 µm; (e) Amber, 75°, 1000 µm; and (f) Tough, 90°, 1000 µm. All the pictures were taken with a 5× microscope objective.

or pillars, that could be applied for circulating tumour cell capturing [26].

A study of the superficial performance of structures was conducted in this work. For this, the topology of the plates shown in Fig. 2b was used. These plates have rectangular and semicircular channels printed (outwards and inwards) on their surface. The main design parameters for these elements (see Fig. 5a) are: i) height (H) and width (W) for rectangular channels (verifying H = W); ii) radius (R) and diameter (D) for semicircular channels (verifying 2R = D); and iii) top diameter ($D_1$), bottom diameter ($D_2$) and height (H) for pillars (verifying $D_1 = D_2 = H$).

As can be seen in Fig. 5, the printed channels show a trapezoidal profile, despite being designed with a CAD rectangular profile. This result is observed both in the outward (Fig. 5b) and inward (Fig. 5c) channels and even in the pillars (Fig. 5d) for all the resins used. To facilitate the interpretation of the data, aspect ratios of the superficial structures printed in Clear resin are plotted in Fig. 6. The chosen ratios were H/W for rectangular channels, 2R/D for semicircular channels and $(2D_2\text{-}D_1)/H$ for pillars. All the channels and pillars were designed with an aspect ratio equal to 1. The deviation from 1 is an indicative of the extent that the structures differ from the original design. In Fig. 6, each subfigure presents the aspect ratios corresponding to the three orientations indicated in Fig. 2c–e: A (red dot), B (blue star) and C (green square).

Two printing regimes were observed for outward rectangular channels (Fig. 6a). First, small channels (0–500 µm) show an aspect ratio that increases with the theoretical width. For these cases, the ratio value is low and does not even reach 0.75 until 500 µm, where orientations A and B obtain their best performance. In this case, for orientation A, with an aspect ratio of 0.75, the printing accuracy (defined as the percentage ratio between the printed result and the designed structure size) is 101% in height and 153% in width. Until now, orientation A showed the higher aspect ratio, followed by C and B (0.69 and 0.66 for 500 µm, respectively), but this scenario changes for larger channels (500–1000 µm), where the observed tendency differs: orientation A stabilizes around 0.70 aspect ratio, while C reaches to 0.8. Orientation B gets its best result for 500 µm and shows the lowest aspect ratio (0.63) of the three printing orientations for a theoretical width of 1000 µm. As observed, the rectangular outward channels did not reach an aspect ratio of 1, indicating that no channel as high as wide was printed.

For inward rectangular channels, two regimes can be also identified (see Fig. 6b). For small channels (0–500 µm), the aspect ratio cannot exceed 0.5, although it continues increasing as the theoretical width does. In this regime, orientation B provides a higher ratio (0.47 for 300 µm), followed by C and A (0.37 and 0.30 for 300 µm, respectively), in contrast to the previous case. For larger channels (500–1000 µm), a performance gap is observed, with all aspect ratios being above 0.75 showing a decreasing trend especially pronounced for orientation A. For channels with a theoretical width of 700 µm, the three orientations practically reach a ratio of 1. Orientation B stands out in this case, reaching a 0.99 aspect ratio and a printing accuracy of 95% in height and 96% in width. For this reason, inward channels represent an improvement in the global aspect ratio for rectangular channels, especially in the range between 700 µm and 1000 µm of width, were they all are near to 1.

For outward pillars, a bottom diameter greater than the top diameter is observed in all cases (Fig. 6c), causing the aspect ratio to be greater than 1 for all the theoretical heights. This phenomenon is more pronounced for small heights (0–500 µm), in which the profile of the pillar is smoothed, reaching a hemisphere shape (in a limit case), with an aspect ratio between 2 and 6. For larger heights (500–1600 µm), all ratios remain between 1 and 2, showing orientation A the best result. A ratio of 1.12 and a printing accuracy of 104% in height, 110% in bottom diameter and 102% in top diameter was observed for this orientation and a theoretical height of 1600 µm, followed by C and B (1.22 and 1.40, respectively). Wells (inward pillars) did not form correctly, so that the correct identification and measurement of their main parameters could not be performed. The concrete details of this phenomenon will be discussed later.

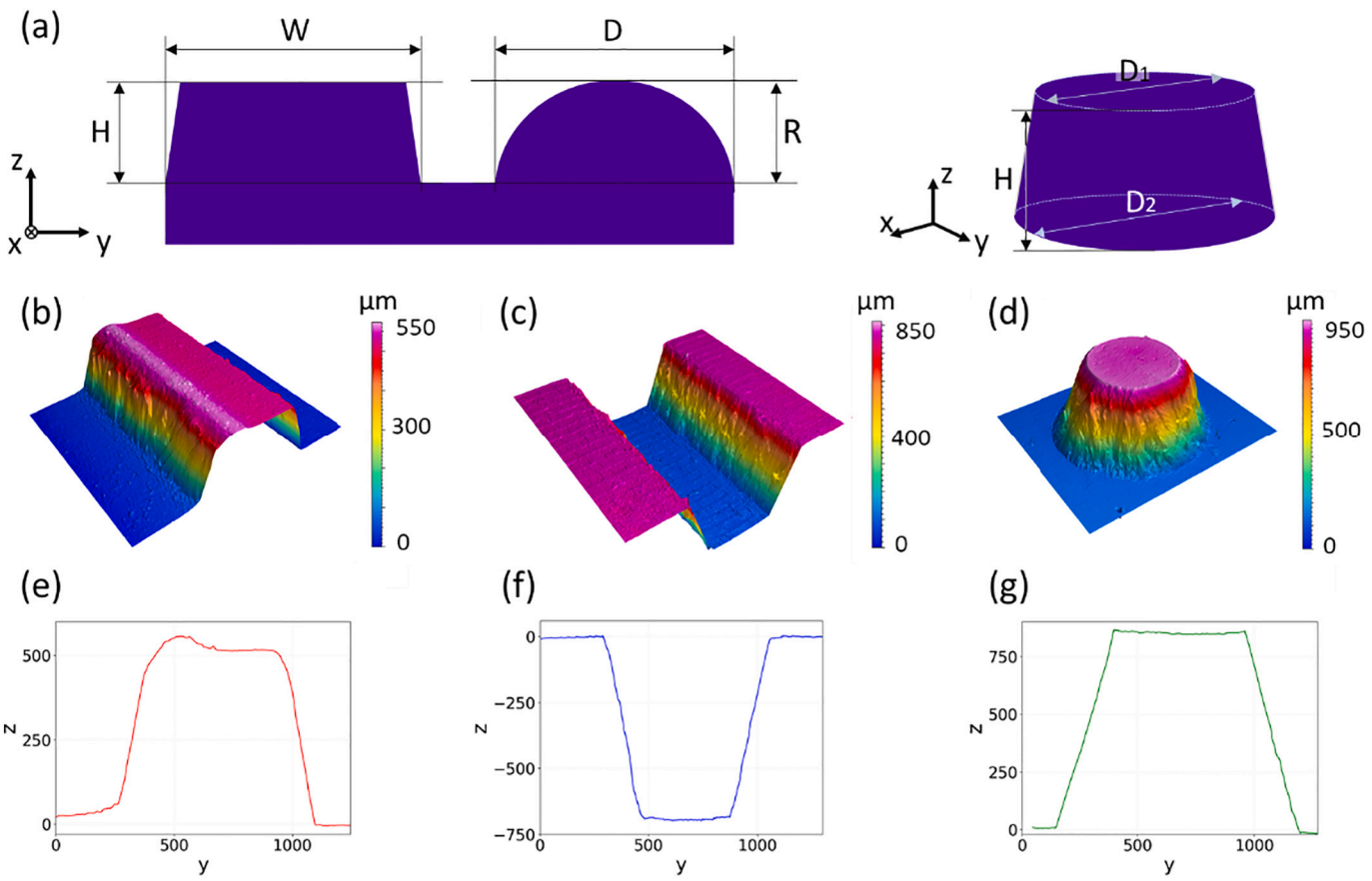


**Fig. 5.** Typical parameters of (a) superficial channel and pillars. Design of rectangular channels verify H = W, semicircular channels verify R = D/2 and pillars $D_1 = D_2 = H$. Confocal images for illustration of (b) outward channel fabricated with the Model resin and (e) its corresponding profile, (c) inward channel fabricated with the Clear resin and (f) its corresponding profile, and (d) outward pillar fabricated with the Dental resin and (g) its corresponding profile. All the pictures were taken with a 10× confocal microscope objective.

For outward semicircular channels, the observed trend is unique since the aspect ratio grows as the theoretical diameter increases for all studied orientations (Fig. 6d). Anyway, two different trends can be described depending on whether the aspect ratio deviates more than 0.25 from 1, and therefore defining two regimes. For small diameters (0–500 µm), channels are below an aspect ratio of 0.75, except for the orientation A, which manages to reach 0.76 for 500 µm. For larger diameters (500–1500 µm), channels are formed with an aspect ratio between 0.75 and 1.25. Orientation A stands out for diameters of 1500 µm, reaching a ratio 0.93 and a printing accuracy of 100% in height and 107% in diameter.

Finally, for inward semicircular channels (Fig. 6e), no orientation exceeds an aspect ratio of 0.75 before 500 µm in diameter, except orientation B for 300 µm. For diameters greater than 500 µm, the ratio tendency changes, going from increasing for all the orientations to stabilizing around to 0.85 for B, increasing slightly for A and stabilizing before growing for C. The closest ratio to 1 is measured for orientation A at 1500 µm in diameter, achieving a value of 0.98 and a printing precision of 95% in height and 98% in diameter.

However, no information about the appearance of the surfaces can be extrapolated from the aspect ratios, since they only offer information about the deviation from the original rectangular, semicircular or cylindrical designed profile. Fig. 7 shows optical microscope images of the inward channels and wells printed for Clear resin at A (left), B (middle) and C (right) orientations. Although the top diameters of the wells are formed correctly (Fig. 7a–c), maintaining a constant radius with a regular border for all the orientations, the same does not applies to their bottom diameter (Fig. 7d–f). The removal of uncured resin did not occur properly during the printing process, promoting its accumulation inside the wells and causing that the cylindrical profile of the structures could not be measured (as mentioned above). This effect explains that the border of the bottom diameter of the well printed at orientation A cannot be identified (Fig. 7d), since the uncured resin was homogeneously deposited, curving the walls. This phenomenon is even more noticeable for wells printed with an inclination respect to the base since the resin can be seen accumulated on the side (Fig. 7e) or top (Fig. 7f) wall of the wells.

This unwanted accumulation of resin can also be observed for inward channels, although its impact can be minimized by choosing a suitable inclination. In the first place, for pieces printed with orientation A, the accumulation of resin occurs homogeneously in the walls (Fig. 7g), although its presence does not significantly affect the profile given the original curved shape (for semicircular channels). On the other hand, for channels printed with orientation B, the uncured resin produces a large profile loss from the surface (Fig. 7h) to the bottom (Fig. 7i) of rectangular channels, since the resin is deposited all along of one of the walls. This orientation produces the largest deviations from an ideal channel, so it is not recommendable to use it for inward channels, whether rectangular or semicircular. Finally, orientation C stands out as the most advisable orientation, since the accumulation of the resin will only occur at the end of the channel, leaving the intermediate region free of obstructions and maintaining the appropriate profile (Fig. 7j) to the extent indicated in Fig. 6b and e.

In summary, the inclination is critical for small and inward structures when evacuating the resin, whose viscosity helps it to accumulate in regions where a sudden change in profile takes place. The evacuation is

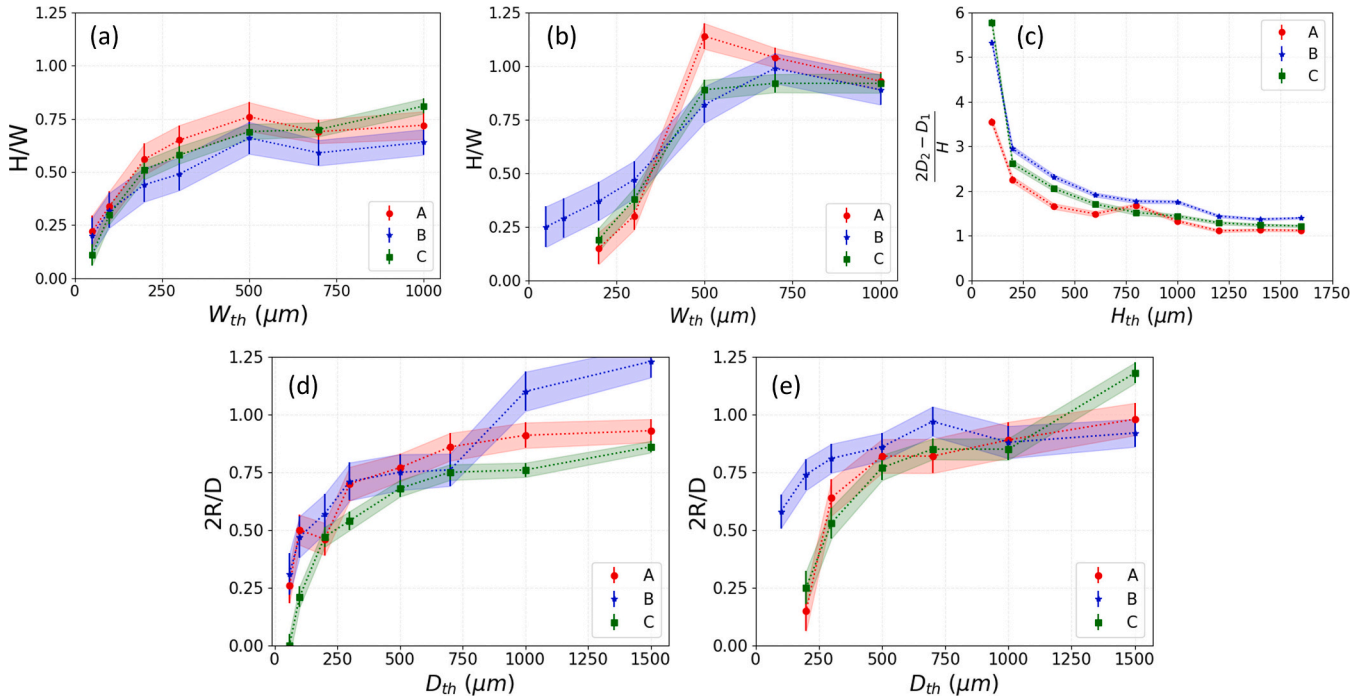


**Fig. 6.** Aspect ratios obtained for the surface structures printed in Clear resin corresponding to: (a) outward and (b) inward rectangular channels; (c) outward pillars; (d) outward and (e) inward semicircular channels. Structures were designed on the surface of plates printed at: orientation A (red dot); orientation B (blue star) and orientation C (green square), as shown in Fig. 2c–e. $W_{th}$, $H_{th}$ and $D_{th}$ denote the theoretical weight, height, and diameter, respectively. (For interpretation of the references to colour in this figure legend, the reader is referred to the web version of this article.)

largely determined by gravity, and a correct orientation (with channels perpendicular to the base) will favour resin to accumulate in areas whose profile is not so valuable, such as the end of the channels, in which microfluidic connectors are generally placed.

Fig. 8 shows FESEM images of selected outward channels printed in different resins at orientation C. Clear resin allows the formation of outward channels with a suitable topology for microfluidic applications: the edges of the channels are well defined (Fig. 8a and b), the surface is smooth ($S_a$ = 1.281 ± 0.306 μm) (Fig. 8c), and the working range adequately goes from hundreds of microns to several millimetres (see Fig. 6a and d). Channels printed on the Model resin also seem suitable for use in microfluidics (Fig. 8d) although its surface finishing is slightly less smooth ($S_a$ = 1.444 ± 0.247 μm) (Fig. 8f) than that obtained for Clear resin(Fig. 8c), which may not be advisable for certain applications such as cell growth, where surface roughness is decisive [27]. The same occurs if the channel is intended to replicate (main use of outward channels) using a transparent polymer, since this roughness can affect the subsequent optical inspection. Definitely, these two resins offer the best surface finishing and lowest roughness, which can be explained taking into consideration the fact that they offer the lowest MTL of all studied resins (as indicated in Table 2): 25 μm. For resins with a higher MLT, as Amber ($S_a$ = 1.977 ± 0.187 μm) (Fig. 8g–i) and Tough ($S_a$ = 3.736 ± 0.713 μm) (Fig. 8j–l), the z-step (50 μm) begins to be noticeable on their surface. This effect may not be very critical for channels that are large enough compared to the step (Fig. 8g), but it can create wavy borders for channels with a diameter in the same order of magnitude (Fig. 8j). The Amber resin also shows a high flaking in the top region of the channel, very pronounced at its end (Fig. 8h). Certain irregularities can also be observed on the top region of channels printed in Tough resin (Fig. 8k). Flexible resin, despite offering the same z-step of 50 μm and an intermediate roughness ($S_a$ = 2.723 ± 0.239 μm), produces more bent channels than these two resins, producing even not straight channels for orientation A. This is due to its deformability, which makes it very vulnerable to the stresses produced during printing process and translates into an inability to reach the goal accuracy of this study. Finally, Dental ($S_a$ = 4.296 ± 1.047 μm) and Elastic ($S_a$ = 8.280 ± 1.738 μm) resins, with a 100 μm z-step are limited from start to only form large channels since the step is very noticeable for structures under few hundred microns.

### 3.5. Replicability

Sometimes it is important to produce a master for posterior replication. In this section, the possibilities that resins offer as materials to manufacture master elements and the quality of the replications obtained from the printed master are analysed. For this, the outward channels fabricated in Section 3.3 were replicated by soft lithography of PDMS, creating cavities in the polymer.

Some resins showed poor performance in replicating PDMS, so not all of them could be used as master. This is the case with Amber (Fig. 9a–c) and Dental (Fig. 9d–f) resin. In Fig. 9b the two most interesting regions for replication analysis are highlighted: the bottom of the channels and the base region. For the bottom, many irregularities and micro-cracks were produced during the soft lithography replication of these resins (Fig. 9c and f), causing that the original topology of the channels could not be transmitted to the replica. The same occurs for the base regions that despite being originally flat, show a high irregularity and flaking when replicated, especially noticeable in the case of Dental resin (Fig. 9d–e). For Flexible and Elastic resins, the replication process cannot be studied since the polymer did not even cure for the temperature and time applied to the other resins (indicated in Section 2.2). The PDMS layer deposited on these resins showed a semi-liquid state that made it impossible to observe the topology of study. These reasons make not convenient the use of the four resins for master manufacturing.

However, three other studied resins allowed a high-quality PDMS replication from masters made of: Clear, $S_a$ = 1.478 ± 0.355 μm (Fig. 10a–c); Model, $S_a$ = 1.672 ± 0.633 μm (Fig. 10d–f); and Tough, $S_a$ = 3.831 ± 0.487 μm (Fig. 10g–i). For them, the polymer surface managed to reproduce the respective surface pattern and a very similar roughness, so that an almost exact replica was obtained. In this scenario,

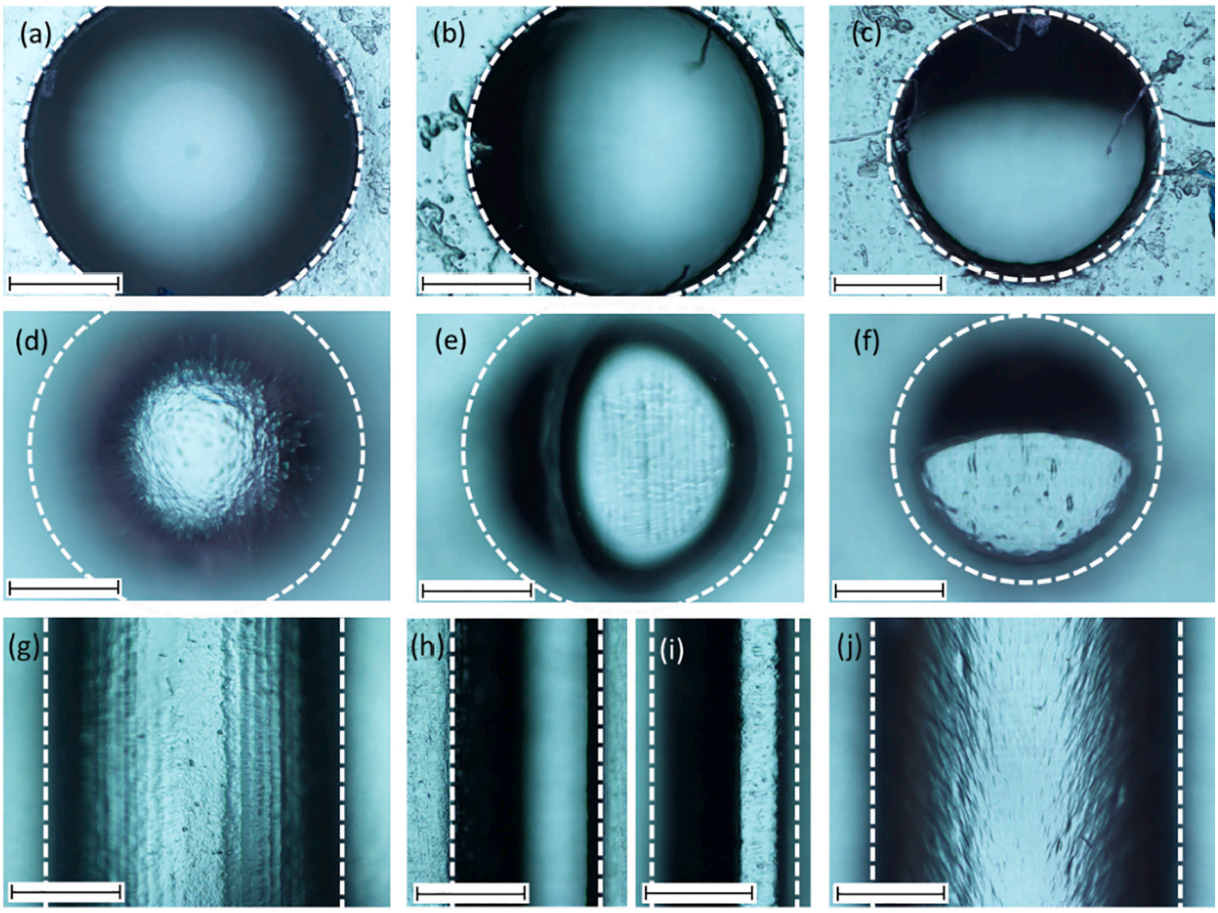


**Fig. 7.** Optical microscope images of inward structures printed for Clear resin. Pictures of top and bottom (respectively) surfaces of the wells printed at: (a), (d) orientation A; (b), (e) orientation B; and (c), (f) orientation C. (g) Picture of the bottom surface of semicircular channel printed at orientation A. Picture of the (h) top and (i) bottom surfaces of rectangular channel printed at orientation B. (j) Picture of the bottom surface of semicircular channel printed at orientation C. All the pictures were taken with a 5× microscope objective. Scale bar 500 μm.

the quality of the PDMS channel will depend only on the quality of master, so all the previous study and optimization of the printer performance can be transferred to the replicated channel.

An EDX analysis of the surfaces of the replicated channels in PDMS was performed to determine if there are any transference of the resin to the PDMS during the soft lithography. Fig. 11 shows the EDX spectra obtained for the three regions of the PDMS replica obtained from a Tough resin master: i) base region (Fig. 11a), ii) bottom of the channel (Fig. 11b) and iii) visible impurities (Fig. 11c). For the bottom of the channels and base regions of PDMS, the analysis showed approximately the same weight percentage of C (40%), Si (35%) and O (25%). The obtained spectra were quite similar for the rest of the replicas. These results agree with the elements that form the polymer ($C_2H_6OSi$). The used equipment cannot detect elements lighter than Be, which explains the absence of H in the spectrum. Moreover, the measurement of the various observed impurities on the replicated surfaces yielded a result similar to the previous spectrum except for the presence of N, that varied depending on the master resin, being 1.5% for Amber, 3.2% for Tough and 4.3% for Clear resin. The presence of these contaminants could come from the N originally present in the resins. Thereby, a transfer of impurities from the master to the replica produced during the soft lithography process was detected. The extent to which this contamination may be critical to the proper functioning of a microfluidic device should be assessed in each specific case.

### 3.6. Biocompatibility

Once all the aspects related to the manufacture of channels to obtain the most precise and physiologically mimetic results (for both direct printing and replication) are analysed, it is necessary to focus on the study of a critical aspect for the correct performance of printed microfluidic devices for biological and biomedical applications: biocompatibility.

Biocompatibility can be tested at different levels attending to the category of body contact (from transient-contacting to implant devices) and to the evaluation process (physicochemical or biological analysis). In the case of microfluidic devices printed for biological or biomedical investigation, the possibility of inclusion of mammalian cells is of particular importance. Therefore, the materials and the finishing should guarantee cell adhesion and viability. In this work, a study on the cell viability of HUVEC was carried out, given its great potential in microfluidic applications in the field of cardiovascular diseases [28].

HUVEC were cultured (10,000 cells/$cm^2$) on plastic (Fig. 12a) and on the three polished resins: Amber (Fig. 12b), Dental (Fig. 12c) and Clear (Fig. 12d). The cells were also seeded on the unpolished surfaces of the same resins (Fig. 12e–g), but the surface roughness avoided a correct observation. After 4 h of seeding, cells were inspected on an optical microscope to test their adhesion. This time is enough for HUVEC to adhere to the surface of culture and to spread through it, as normally observed under standard conditions on plastic material. Amber, Dental, and Clear resins showed similar behaviour to HUVEC adhesion.

After adhesion, HUVEC in an appropriate cell growth medium start

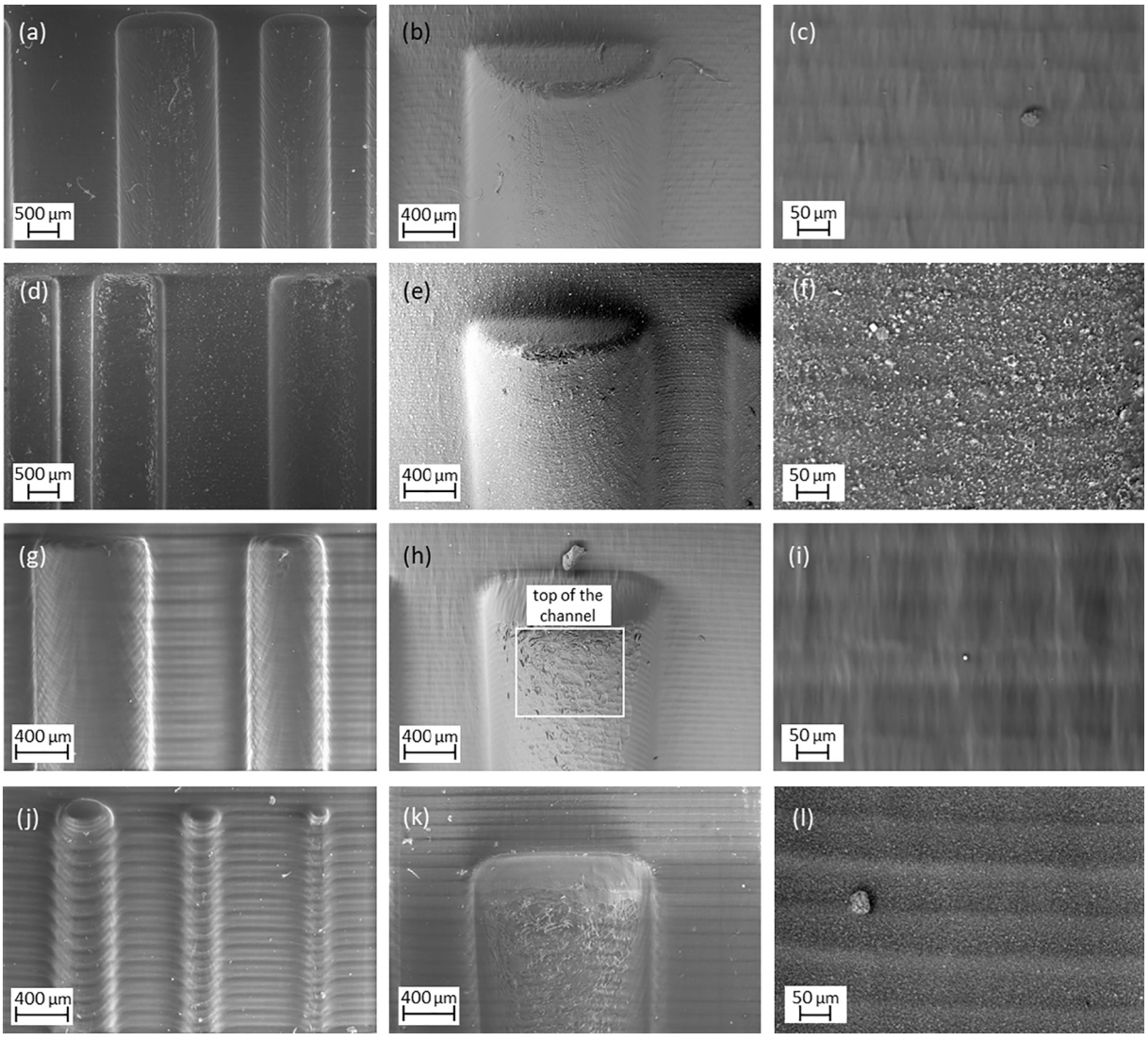


**Fig. 8.** FESEM images of the 3D superficial outward channels printed in (a), (b), (c) Clear; (d), (e), (f) Model; (g), (h), (i) Amber and (j), (k), (l) Tough resin. Pictures were taken with the following microscope objectives: a) and d) 50×; b), e), g), h), j) and k) 100×; and c), f), i) and l) 500×.

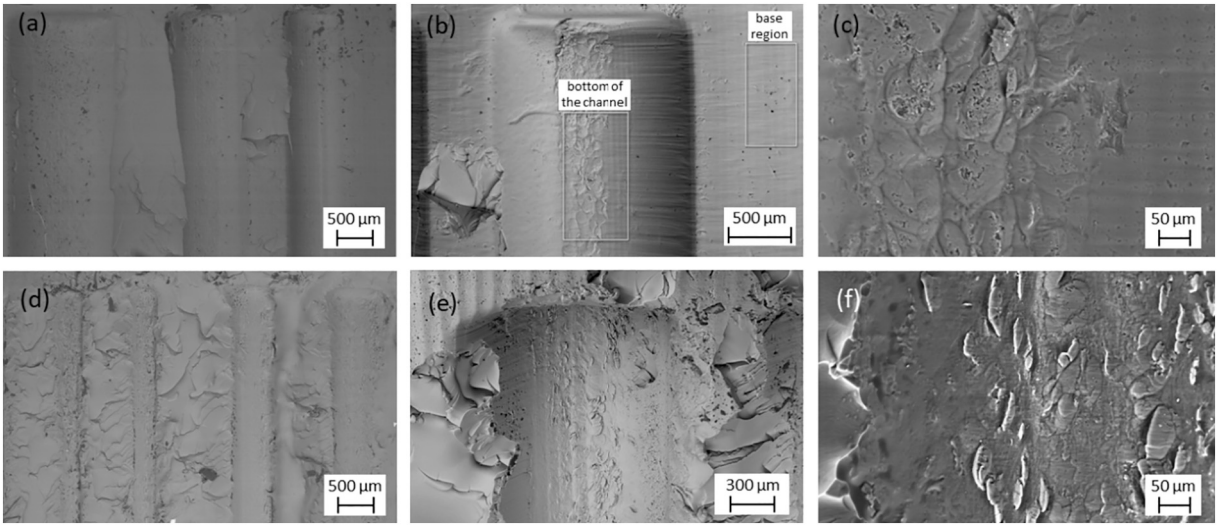


**Fig. 9.** SEM images of PDMS soft lithography replicas of superficial channels printed in (a), (b), (c) Amber and (d), (e), (f) Dental resin. The PDMS replicated inward channels show a poor replication performance. Pictures were taken with the following microscope objectives: a) and d) 50×; b) and e) 100×; and c) and f) 500×.

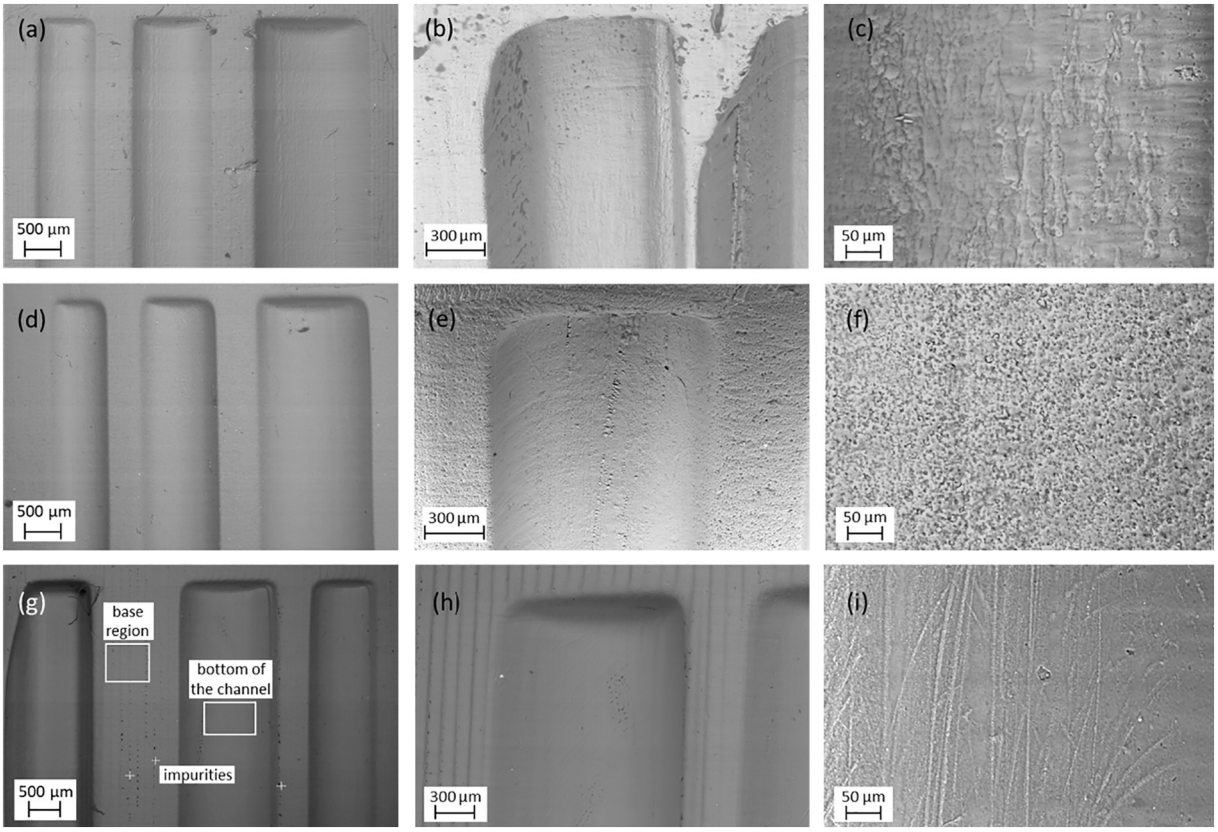


**Fig. 10.** SEM images of PDMS soft lithography replicas of superficial channels printed in (a), (b), (c) Clear; (d), (e), (f) Model and (g), (h), (i) Tough resin. Regions analysed by EDX are also highlighted. The PDMS replicated inward channels show a good replication performance. Pictures were taken with the following microscope objectives: a) and d) 50×; g) 45×; b) and e) 150×; h) 100×; and c), f) and i) 500×.

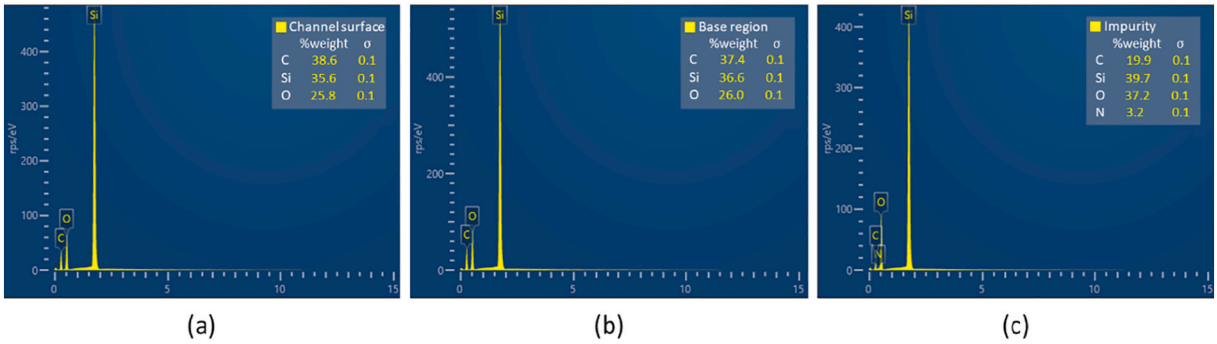


**Fig. 11.** EDX spectra of the (a) channel surface, (b) base region and (b) impurity observed on the PDMS replica obtained from a Tough resin master.

to divide, forming colonies of cells than in these conditions will expand over the surface of culture until form a confluent monolayer with cells in a hexagonal or cuboidal form with large nuclei. If culture is maintained, cells will adopt a cobblestone-shaped layer, simulating the morphology of the endothelium in vivo [29].

Cell viability over the different surfaces was tested with a fluorescent dye for living cells (Fig. 13). Calcein AM is a cell-permeant molecule that is converted in a fluorescent dye by the intracellular esterases in living cells. Thereby, HUVEC were stained after several hours of culture and their evolution was followed until 24 h after seeding. Despite a similar adhesion was observed in the Amber, Clear and Dental resins, the evolution of the cultures was different. On Dental (Fig. 13c) and Clear (Fig. 13d) resins, HUVEC did not increase their cellular surface and there was no significant cell growth after 24 h post-seeding (Table 3). HUVEC maintained constricted their proportions and colonies of cells seemed not to evolve. On the other hand, a different behaviour was observed in the Amber resin (Fig. 13b). In this case, after 24 h of culture, HUVEC maintained their spread as observed in the control experiments over plastic surface (Fig. 13a) and the mean cell surface was even larger, indicating a good adaptation to the surface. Colonies of cells also grew, and the culture progressed to confluence in a similar extent than the control experiment over conventional plastic material. Note that although the growth is lower in number of cells, the cell area increases (Table 3).

In conclusion, although the resins Clear and Dental showed biocompatibility to HUVEC in terms of cell adhesion, it seems that only Amber resin gathers the characteristics needed to guarantee HUVEC adhesion to the surface and the progression and maintenance of the HUVEC culture over the time. These results partially agree with previous work of Kreß et al. [30], where they observed a bad biocompatibility of

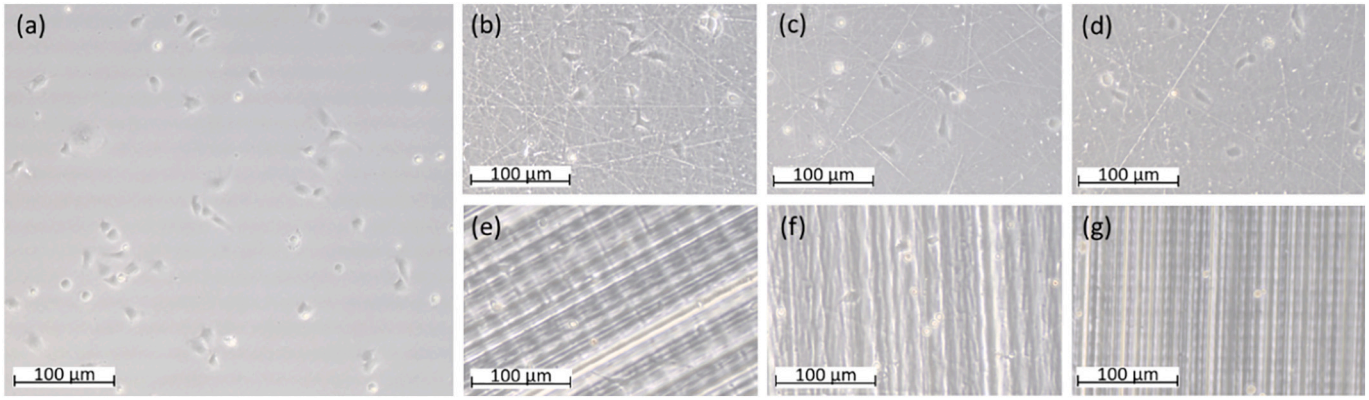


**Fig. 12.** Representative optical microscope images of HUVEC cultures on (a) plastic control dishes and on the polished (top) and unpolished (bottom) surface of (b), (e) Amber; (c), (f) Dental and (d), (g) Clear resin. The images were acquired 4 h after cell seeding. All the pictures were taken with a 100× magnification.

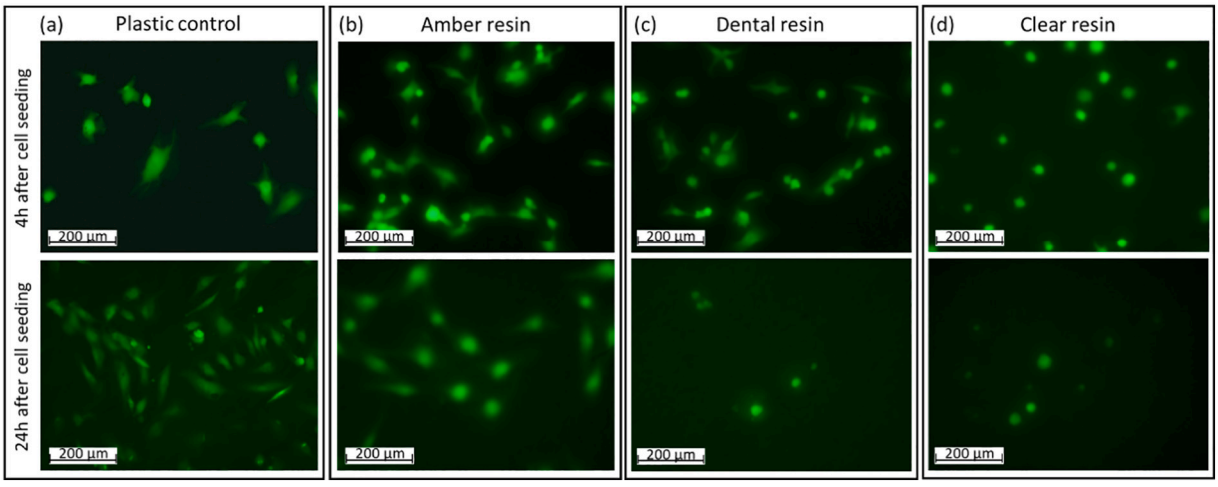


**Fig. 13.** Representative fluorescence microscope images of HUVEC cultures with life-staining calcein AM on the polished surface of (a) standard plastic, (b) Amber, (c) Dental and (d) Clear resins. The images were acquired 4 h (top) and 24 h (bottom) after cell seeding. All the pictures were taken with a 100× magnification.

**Table 3**
Cell growth after 24 h of culture measured as percentage of cells numbers and area of the cells. *p < 0.005 with respect to control, using Student's t-test.

| Resin | Culture growth at 24 h (%) | Cell area ($\mu m^2$) |
|---|---|---|
| Control (polystyrene) | 479.7 ± 49.3 | 499.9 ± 86.2 |
| Amber | 165.2 ± 45.1* | 940.8 ± 5.9* |
| Clear | −39.2 ± 2.1* | 629.3 ± 20.0 |
| Dental | 39.1 ± 27.6* | 690.4 ± 3.3 |

Clear resin with human adipose-derived mesenchymal stem cells, but a relatively acceptable compatibility for Dental LT resin. However, biocompatibility depends not only on the material used, but also on the type of cells employed for the assay. On this regard, Hart et al. observed better compatibility for Clear resin than for Dental LT, using HL-1 cells [31]. These cells are derived from rat atrial cardiac myocytes. Altogether suggests that the confirmation of biocompatibility should be done for each type of cells and in the optimal conditions of culture.

## 4. Conclusions

Microfluidics is a field that requires multidisciplinary technologies capable of manufacturing highly detailed structures in a repeatable and precise way. 3D printing has a short but promising path in this area, democratizing access to manufacturing techniques through simple procedures and very low waste production. In particular, SLA printers stand out thanks to recent developments in laser technologies, which make them the most extended option capable of achieving greater precision within the current additive manufacturing technologies. In this work, the most important functionalities for manufacturing solvent microfluidic devices are tested for the first time using a Low Force Stereolithography (LFS) technique. A set of seven printing resins (Clear, Dental, Tough, Amber, Flexible, Elastic and Model) was studied according to the needs of most of the microfluidic devices used for biological and biomedical research.

A unique piece containing several structures used in microfluidic devices, such as superficial channels (inward and outward), internal channels and pillars was designed. The most important features: range of dimensions and accuracy, time of printing, transparency and biocompatibility of the materials used were studied.

We can conclude that Dental resin required the shortest printing time, followed by Amber and Flexible while Model and Clear resin, printed at the maximum resolution, took the longest one. The transmission spectra of the transparent resins were measured. It was found that polishing increases the transmittance for Amber, Clear and Dental resins, reaching around 80% transmittance for the visible range, where fluorescence microscopy excitation lengths are typically found.

Regarding the formation of internal channels, the accumulation of resin was found to be a determining factor in causing obstructions and malformation of the channels. To avoid this phenomenon, two aspects were crucial: the diameter of the channels and their printing orientation.

While for channels with a diameter less than 500 μm obstructed lumen were formed, for greater diameter values, an open lumen was obtained. For angles greater than 60° and diameters greater than 500 μm, resins such as Dental or Amber managed to form channels with a printing accuracy over 80%. For larger diameters (1000 μm), the accuracy was >70% and continued to increase with the angle. For channels of 1500 μm in diameter, all the resins studied achieved an accuracy >90%. The surface performance of the printer was also analysed by studying the topology of a series of channels and pillars printed inwards and outwards. The fabricated structures showed certain deviations compared to the designed ones that were quantified by various aspect ratios. Taking Clear resin as an example, it was observed that the ratios almost reached 1 as the channels increased in size. In general, two printing regimes can be distinguished for channels. Small channels (0–500 μm) deviate significantly from the designs with aspect ratios below 0.75, since the resolution of the printer is not capable of forming such small structures. For larger channels (500–1500 μm), the ratios obtained were between 0.75 and 1.25. All the analysed resins follow a similar behaviour, and their accuracy is determined by the MTL, where Clear and Model resins stand out. The surface finishing of the structures was also assessed. For the inward ones, it was found that printing orientation is critical and can favour unwanted accumulation of resin on the sides of the channels and wells. Channels manufactured with an orientation perpendicular to the base showed the best uncured resin evacuation.

Manufacturing of structures made up of resins to be used as masters was also analysed. Clear, Model and Tough resin showed a good performance when the material used for soft lithography replication was PDMS. On the contrary, a poor transference of the original topology was observed for Amber and Dental resins. The polymer did not cure on the Flexible and Elastic resins, so we can conclude that these resins are not convenient for master manufacturing.

Finally, the biocompatibility study with HUVEC revealed different behaviour for each resin. Whereas the three resins, Amber, Dental and Clear allowed the adhesion of HUVEC to their polished surfaces to a similar extent, cell growth after 24 h was not observed in all the resins. HUVEC were not able to grow over Dental and Clear resins and after 24 h the culture did not progress. On the contrary, HUVEC grew over Amber resin to a similar extent that cultures made over conventional plastic material. Therefore, Amber showed an adequate biocompatibility, in terms of cell adhesion and cell growth for HUVEC.

## CRediT authorship contribution statement

**Bastián Carnero:** Conceptualization, Validation, Writing - Original Draft preparation, Investigation. **Carmen Bao-Varela:** Conceptualization, Validation, Writing - Review & Editing. **Ana Isabel Gómez-Varela:** Resources, Visualization. **Ezequiel Álvarez:** Conceptualization, Methodology. **María Teresa Flores-Arias:** Conceptualization, Supervision, Funding acquisition.

## Declaration of competing interest

The authors declare that they have no known competing financial interests or personal relationships that could have appeared to influence the work reported in this paper.

## Acknowledgements

Authors gratefully thank contracts AEI RTI2018-097063-B-100, AEI/FEDER, UE; ED431B 2020/29; ED431E 2018/08 and ED481D-2021-019, Consellería de Educación Xunta de Galicia/FEDER e Estructuración Xunta de Galicia, IN607A2019-02 and Sociedad española de cardiología y Fundación español del corazón, SEC/FEC-INV-BAS 20/013.

## References

[1] G. Bull, J. Groves, The Democratization of Production, Learn. Lead. With Technol. 37, 2009, pp. 36–37. http://www.eric.ed.gov/ERICWebPortal/recordDetail?accno=EJ863943.
[2] A.I. Shallan, P. Smejkal, M. Corban, R.M. Guijt, M.C. Breadmore, Cost-effective three-dimensional printing of visibly transparent microchips within minutes, Anal. Chem. 86 (2014) 3124–3130, https://doi.org/10.1021/ac4041857.
[3] B.S. Rupal, E.A. Garcia, C. Ayranci, A.J. Qureshi, 3D printed 3D-microfluidics: recent developments and design challenges, J. Integr. Des. Process. Sci. 22 (2019) 5–20, https://doi.org/10.3233/jid-2018-0001.
[4] Y.Y. Chen, B.R. Kingston, W.C.W. Chan, Transcribing in vivo blood vessel networks into in vitro perfusable microfluidic devices, Adv. Mater. Technol. 5 (2020), 2000103, https://doi.org/10.1002/admt.202000103.
[5] R.H. Liu, M.A. Stremler, K.V. Sharp, M.G. Olsen, J.G. Santiago, R.J. Adrian, H. Aref, D.J. Beebe, Passive mixing in a three-dimensional serpentine microchannel, J. Microelectromech. Syst. 9 (2000) 190–197, https://doi.org/10.1109/84.846699.
[6] H. Nabesawa, T. Hitobo, S. Wakabayashi, T. Aasji, T. Abe, M. Seki, Polymer surface morphology control by reactive ion etching for microfluidic devices, Sensors Actuators B Chem. 132 (2008) 637–643, https://doi.org/10.1016/j.snb.2008.01.050.
[7] C. Liu, Y. Liao, F. He, Y. Shen, D. Chen, Y. Cheng, Z. Xu, K. Sugioka, K. Midorikawa, Fabrication of three-dimensional microfluidic channels inside glass using nanosecond laser direct writing, Opt. Express 20 (2012) 4291, https://doi.org/10.1364/OE.20.004291.
[8] C.S. Carrell, C.P. McCord, R.M. Wydallis, C.S. Henry, Sealing 3D-printed parts to poly(dimethylsiloxane) for simple fabrication of microfluidic devices, Anal. Chim. Acta 1124 (2020) 78–84, https://doi.org/10.1016/j.aca.2020.05.014.
[9] V. Romanov, R. Samuel, M. Chaharlang, A.R. Jafek, A. Frost, B.K. Gale, FDM 3D printing of high-pressure, heat-resistant, transparent microfluidic devices, Anal. Chem. 90 (2018) 10450–10456, https://doi.org/10.1021/acs.analchem.8b02356.
[10] O. Moreno-Rivas, D. Hernández-Velázquez, V. Piazza, S. Marquez, Rapid prototyping of microfluidic devices by SL 3D printing and their biocompatibility study for cell culturing, Mater. Today Proc. 13 (2019) 436–445, https://doi.org/10.1016/j.matpr.2019.03.189.
[11] S. Knowlton, C.H. Yu, F. Ersoy, S. Emadi, A. Khademhosseini, S. Tasoglu, 3D-printed microfluidic chips with patterned, cell-laden hydrogel constructs, Biofabrication. 8 (2016) 1–13, https://doi.org/10.1088/1758-5090/8/2/025019.
[12] B. Heidt, R. Rogosic, S. Bonni, J. Passariello-Jansen, D. Dimech, J.W. Lowdon, R. Arreguin-Campos, E. Steen Redeker, K. Eersels, H. Diliën, B. van Grinsven, T. J. Cleij, The liberalization of microfluidics: form 2 Benchtop 3D printing as an affordable alternative to established manufacturing methods, Phys. Status Solidi (2020), 1900935, https://doi.org/10.1002/pssa.201900935.
[13] D.A. Zopf, S.J. Hollister, M.E. Nelson, R.G. Ohye, G.E. Green, Bioresorbable airway splint created with a three-dimensional printer, N. Engl. J. Med. 368 (2013) 2043–2045, https://doi.org/10.1056/NEJMc1206319.
[14] G. Comina, A. Suska, D. Filippini, Low cost lab-on-a-chip prototyping with a consumer grade 3D printer, Lab Chip 14 (2014) 2978–2982, https://doi.org/10.1039/C4LC00394B.
[15] J.A. Barron, P. Wu, H.D. Ladouceur, B.R. Ringeisen, Biological laser printing: a novel technique for creating heterogeneous 3-dimensional cell patterns, Biomed. Microdevices 6 (2004) 139–147, https://doi.org/10.1023/B:BMMD.0000031751.67267.9f.
[16] Y. Alapan, M.N. Hasan, R. Shen, U.A. Gurkan, Three-dimensional printing based hybrid manufacturing of microfluidic devices, J. Nanotechnol. Eng. Med. 6 (2015) 1–9, https://doi.org/10.1115/1.4031231.
[17] S.V. Murphy, A. Atala, 3D bioprinting of tissues and organs, Nat. Biotechnol. 32 (2014) 773–785, https://doi.org/10.1038/nbt.2958.
[18] A.K. Au, W. Lee, A. Folch, Mail-order microfluidics: evaluation of stereolithography for the production of microfluidic devices, Lab Chip 14 (2014) 1294–1301, https://doi.org/10.1039/C3LC51360B.
[19] Y. Hwang, O.H. Paydar, R.N. Candler, 3D printed molds for non-planar PDMS microfluidic channels, Sensors Actuators A Phys. 226 (2015) 137–142, https://doi.org/10.1016/j.sna.2015.02.028.
[20] H.N. Chan, Y. Chen, Y. Shu, Y. Chen, Q. Tian, H. Wu, Direct, one-step molding of 3D-printed structures for convenient fabrication of truly 3D PDMS microfluidic chips, Microfluid. Nanofluid. 19 (2015) 9–18, https://doi.org/10.1007/s10404-014-1542-4.
[21] Introducing the Form 3 and Form 3L, Powered by Low Force Stereolithography, (n. d.). https://formlabs.com/blog/introducing-form-3-form-3l-low-force-stereolithography/, (Accesed April 2021).
[22] J.C. McDonald, D.C. Duffy, J.R. Anderson, D.T. Chiu, H. Wu, O.J.A. Schueller, G. M. Whitesides, Fabrication of microfluidic systems in poly(dimethylsiloxane), Electrophoresis. 21 (2000) 27–40, https://doi.org/10.1002/(sici)1522-2683(20000101)21:1<27::aid-elps27>3.3.co;2-3.
[23] K. Raj M, S. Chakraborty, PDMS microfluidics: a mini review, J. Appl. Polym. Sci. 137 (2020) 1–14, https://doi.org/10.1002/app.48958.
[24] B. Paradela-Dobarro, B.K. Rodiño-Janeiro, J. Alonso, S. Raposeiras-Roubín, M. González-Peteiro, J.R. González-Juanatey, E. Álvarez, Key structural and functional differences between early and advanced glycation products, J. Mol. Endocrinol. 56 (2015) 23–37, https://doi.org/10.1530/JME-15-0031.
[25] A. Urrios, C. Parra-Cabrera, N. Bhattacharjee, A.M. Gonzalez-Suarez, L.G. Rigat-Brugarolas, U. Nallapatti, J. Samitier, C.A. Deforest, F. Posas, J.L. Garcia-Cordero, A. Folch, 3D-printing of transparent bio-microfluidic devices in PEG-DA, Lab Chip 16 (2016) 2287–2294, https://doi.org/10.1039/c6lc00153j.

[26] D. Nieto, R. Couceiro, M. Aymerich, R. Lopez-Lopez, M. Abal, M.T. Flores-Arias, A laser-based technology for fabricating a soda-lime glass based microfluidic device for circulating tumour cell capture, Colloids Surf. B: Biointerfaces 134 (2015) 363–369, https://doi.org/10.1016/j.colsurfb.2015.07.007.
[27] M. Aymerich, D. Nieto, M.T. Flores-Arias, Laser-based surface multistructuring using optical elements and the Talbot effect, Opt. Express 23 (2015) 24369, https://doi.org/10.1364/OE.23.024369.
[28] M. Aymerich, E. Álvarez, C. Bao-Varela, I. Moscoso, J.R. González-Juanatey, M. T. Flores-Arias, Laser technique for the fabrication of blood vessels-like models for preclinical studies of pathologies under flow conditions, Biofabrication. 9 (2017), 025033, https://doi.org/10.1088/1758-5090/aa6c3d.
[29] D.J. Medina-Leyte, M. Domínguez-Pérez, I. Mercado, M.T. Villarreal-Molina, L. Jacobo-Albavera, Use of human umbilical vein endothelial cells (HUVEC) as a model to study cardiovascular disease: a review, Appl. Sci. 10 (2020) 938, https://doi.org/10.3390/app10030938.
[30] S. Kreß, R. Schaller-Ammann, J. Feiel, J. Priedl, C. Kasper, D. Egger, 3D printing of cell culture devices: assessment and prevention of the cytotoxicity of photopolymers for stereolithography, Materials (Basel) 13 (2020) 3011, https://doi.org/10.3390/ma13133011.
[31] C. Hart, C.M. Didier, F. Sommerhage, S. Rajaraman, Biocompatibility of blank, post-processed and coated 3D printed resin structures with electrogenic cells, Biosensors. 10 (2020) 152, https://doi.org/10.3390/bios10110152.